Progress In Electromagnetics Research, Vol. 169, 1–15, 2020

The Multilevel Fast Physical Optics Method for Calculating High Frequency Scattered Fields

Zhi Yang Xue[1], Yu Mao Wu[1, *], Weng Cho Chew[2], Ya Qiu Jin[1], and Amir Boag[3]

Abstract—The multilevel fast physical optics (MLFPO) is proposed to accelerate the computation of the fields scattered from electrically large coated scatterers. This method is based on the quadratic patch subdivision and the multilevel technology. First, the quadratic patches are employed rather than the planar patches to discretize the considered scatterer. Hence, the number of the contributing patches is cut dramatically, thus making the workload of the MLFPO method much lower than that of the traditional Gordon's method. Next, the multilevel technology is introduced in this work to avoid calculating the physical optics scattered fields from the considered scatterer directly, so that the proposed algorithm can significantly reduce the computational complexity. Finally, numerical results have demonstrated the accuracy and efficiency of the MLFPO method based on the quadratic patches.

1. INTRODUCTION

Recently, the electromagnetic (EM) simulation of electrically large coated scatterers attracts more and more attentions [1–5]. In the low- and medium-frequency regimes, several numerical methods, such as the method of moments (MoM) [6–8], the finite element method (FEM) [9], and the finite differences time domain (FDTD) method [10] have been proposed to calculate the EM scattering from the electrically large coated scatterers. However, when a high frequency and electrically large scatterer are considered [11], these methods become unattractive due to their high computational complexity. Fortunately, at such frequencies, the asymptotic techniques, such as the ray based method [12] and the PO-based methods [13–18], become applicable for the scatterers that are large and smooth on the wavelength scale. The ray tracing methods provide a phenomenological solution, cast in terms of the reflected and diffracted ray contributions, but suffer from high sensitivity to geometrical details and occasional failures [19]. Thus, the PO-based approximation is often a preferred high frequency method providing uniform wave solutions, while avoiding the computationally heavy numerically rigorous techniques. The PO approximation is a high frequency method which can get reasonable accuracy when the size of the considered scatterer is much larger than the wavelength. The induced electric and magnetic currents depend on the geometry of the scatterers and the incident wave. One of the assumptions of PO method is that the induced electric and magnetic currents exist only in the lit region of the scatterer. Then, the scattered field produced by the induced surface electric and the magnetic currents can be expressed as surface integrals [20–26], leading to efficient calculation of the PO scattered field.

Gordon [27, 28], and Ludwig [29] made use of the analytical expression to calculate the PO scattered fields through flat patches. This method separates the integration domain into several subdomains on

Received 12 July 2020, Accepted 12 September 2020, Scheduled 6 November 2020

* Corresponding author: Yu Mao Wu (yumaowu@fudan.edu.cn).

[1] Key Laboratory for Information Science of Electromagnetic Waves, School of Information Science and Technology, Fudan University, Shanghai 200433, China. [2] Department of Electrical and Computer Engineering, University of Illinois, Urbana, IL 61801, USA. [3] School of Electrical Engineering, Tel Aviv University, Tel Aviv 69978, Israel.

the order of the 0.1 wavelength. Hence, a simple linear form will be obtained. However, the workload will obviously increase with increasing frequency.

In [30–32], the PO currents can be represented as current mode which can be characterized by the amplitude and the quadratic phase functions that vary slowly over large integration domain. Then, the PO scattered field can be computed from the surface PO currents. This method also can be used to analyze the multiple interaction problems based on the surface current mode.

The numerical efficiency of the computational techniques can be evaluated based on their asymptotic computational complexity [33]. We assume that L is the diameter of the smallest sphere circumscribing the scatterer and $k_{\max}$ is the wavenumber at the highest frequency within the excitation bandwidth. Then, the number of angular sampling points and the frequency sampling points are proportional to the electrical size N of the scatterer, where $N = k_{\max}L$. Accordingly, the number of the far-field points varies from $O(N^2)$ (two-dimensional pattern) to $O(N^3)$ (three-dimensional pattern). After combining the computational complexity of calculating the PO integral, the calculation of the PO scattering data has computational complexities varying from $O(N^4)$ to $O(N^5)$. The workload of this task is very high if N is a large parameter.

When electrically large scatterers are considered, the computation time is often dominated by the PO integration process. The multilevel domain decomposition algorithm proposed in [34, 35], utilizing the domain decomposition and interpolation, aims at achieving a high computational efficiency, i.e., has reduced the complexity from $O(N^4)$ to $O(N^2 \log N)$ for two-dimensional pattern computation (from $O(N^5)$ to $O(N^3)$ for the three-dimensional case). This MLPO algorithm calculates the backscattered field over a range of aspect angles and frequencies accurately and quickly, and can be extended to coated scatterers [33–37]. The method is based on the property that the scattering pattern is a bandlimited function of the angles and frequencies for the finite size scatterers. Hence, the number of the frequency sampling points or angular sampling points at the bottom level is much less than the final one. However, the number of the planar patches modeling the surfaces of the scatterers will increase vastly with the increasing frequency. Therefore, the workload of calculating the PO integrals at the bottom level would increase since the multilevel technology does not reduce the computational complexity for a single observation point.

In order to solve this problem, in this work, we propose the MLFPO method using quadratic patches at the bottom level. Specifically, we use the quadratic (rather than planar) patches to discretize the surfaces of the electrically large coated scatterer. Hence, the number of the quadratic patches is much less than that of planar patches. Next, the PO integrals from each quadratic patch are represented as closed-form formulas with complementary error function method. Therefore, this method can speed up the calculation with necessary accuracy.

The manuscript is organized as follows. The PO scattered fields of coated scatterers are introduced in Section 2. Section 3 gives the generalized reflection coefficients of a multi-layered medium. In Section 4, the quadratic surface subdivision technology and the closed-form formulas with complementary error function are proposed. The multilevel technology is presented in Section 5. In Section 6, the performance of the algorithm in terms of accuracy and efficiency is demonstrated via numerical examples. Section 7 provides the application of the numerical algorithm.

2. THE PO SCATTERED FIELDS OF COATED SCATTERERS

The EM fields scattered from electrically large coated objects can be represented by radiation of the equivalent electric currents $\mathbf{J}$ and magnetic currents $\mathbf{M}$ placed on the exterior surfaces as

$$\mathbf{E}^s(\mathbf{r}) \approx \frac{-ike^{ikr}}{4\pi r} \int_{S_l} \mathbf{r} \times (\mathbf{M} - \eta \mathbf{r} \times \mathbf{J}) e^{-ik\hat{\mathbf{r}}\cdot\mathbf{r}'} dS(r') \tag{1}$$

where

$$\mathbf{J} = \hat{\mathbf{n}} \times \mathbf{H}, \quad \mathbf{M} = -\hat{\mathbf{n}} \times \mathbf{E} \tag{2}$$

$$\mathbf{E} = \mathbf{E}^{inc} + \mathbf{E}^s, \quad \mathbf{H} = \mathbf{H}^{inc} + \mathbf{H}^s \tag{3}$$

Here, $\mathbf{E}$ and $\mathbf{H}$ represent the total electric and magnetic fields, respectively; $\mathbf{E}^{inc}$ and $\mathbf{H}^{inc}$ represent the incident electric and magnetic fields, while $\mathbf{E}^s$ and $\mathbf{H}^s$ represent the scattered electric and magnetic

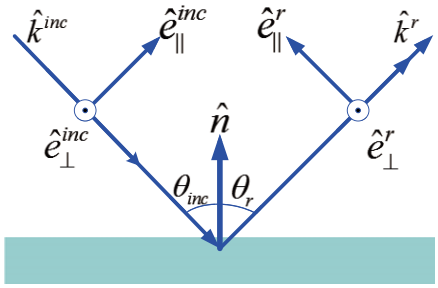

Figure 1. The local coordinate system on the surface of the scatterer.

fields, respectively. Also, $\hat{\mathbf{n}}$ is the outward normal unit vector of the exterior surface, and r and $\hat{\mathbf{r}}$ are the distance and the unit vector between the observation point and the scatterer, respectively. S_l is the lit region of the considered scatterer, and η is the free space intrinsic impedance.

The PO currents on the lit region of the scatterer are obtained using the tangent plane approximation, hence, the local coordinate system is illustrated in Fig. 1. In Fig. 1, $\hat{\mathbf{k}}^{inc}$ is the direction of the incident wave propagation and θ_{inc} is the angle between the incident wave propagation direction and the outward unit normal vector of the exterior surface. $\hat{\mathbf{k}}_r$ is the direction of the reflected wave propagation which follows the Fresnel's law. Here, $\hat{\mathbf{e}}^{inc}_{\parallel}$ and $\hat{\mathbf{e}}^{r}_{\parallel}$ are the parallel polarizations of the incident and reflected electric fields, while $\hat{\mathbf{e}}^{inc}_{\perp}$ and $\hat{\mathbf{e}}^{r}_{\perp}$ are the perpendicular polarizations of the incident and reflected electric fields, respectively. From Fig. 1, the relationship between the propagation direction and the polarization direction can be expressed as

$$\hat{\mathbf{e}}^{inc}_{\parallel} = \hat{\mathbf{e}}^{inc}_{\perp} \times \hat{\mathbf{k}}^{inc}, \quad \hat{\mathbf{e}}^{r}_{\parallel} = \hat{\mathbf{e}}^{r}_{\perp} \times \hat{\mathbf{k}}^{r}, \quad \hat{\mathbf{e}}_{\perp} = \frac{\hat{\mathbf{k}}^{inc} \times \hat{\mathbf{n}}}{\|\hat{\mathbf{k}}^{inc} \times \hat{\mathbf{n}}\|}$$

Therefore, the PO currents on the lit region of the exterior surface of the scatterer can be formulated as

$$\mathbf{M} = e^{i\hat{k}^{inc}\cdot\mathbf{r}'}(-(1+R_{\perp})E_{\perp}(\hat{\mathbf{n}} \times \hat{\mathbf{e}}_{\perp}) + (1-R_{\parallel})E_{\parallel}\cos\theta_{inc}\,\hat{\mathbf{e}}_{\perp}) \tag{4}$$

$$\mathbf{J} = \frac{1}{\eta}\, e^{i\hat{k}^{inc}\cdot\mathbf{r}'}((1-R_{\perp})E_{\perp}\cos\theta_{inc}\,\hat{\mathbf{e}}_{\perp} + (1+R_{\parallel})E_{\parallel}(\hat{\mathbf{n}} \times \hat{\mathbf{e}}_{\perp})) \tag{5}$$

where $E_{\perp}$ and $E_{\parallel}$ are the components of electric fields along the perpendicular and parallel polarization directions; $R_{\perp}$ and $R_{\parallel}$ are the generalized reflected coefficients of the multilayered medium which will be described in the next section.

In order to simplify the scattered field formulations, the PO scattered fields are rewritten as follows

$$\mathbf{E}^s(\mathbf{r}) \approx \int_{S_l} \mathbf{s}(\mathbf{r},\mathbf{r}')e^{-ikv(\mathbf{r},\mathbf{r}')}dS(\mathbf{r}') \tag{6}$$

where

$$\begin{aligned}\mathbf{s}(\mathbf{r},\mathbf{r}') = \frac{-ike^{ikr}}{4\pi r}\,\hat{r} \times \Big\{ &-(1+R_{\perp})E_{\perp}(\hat{\mathbf{n}} \times \hat{\mathbf{e}}_{\perp}) + (1-R_{\parallel})E_{\parallel}\cos\theta_{inc}\,\hat{\mathbf{e}}^{inc}_{\perp} \\ &-\hat{\mathbf{r}} \times \left[(1-R_{\perp})E_{\perp}\cos\theta_{inc}\,\hat{\mathbf{e}}_{\perp} + (1+R_{\parallel})E_{\parallel}(\hat{\mathbf{n}} \times \hat{\mathbf{e}}_{\perp})\right] \Big\}\end{aligned} \tag{7}$$

$$v(\mathbf{r},\mathbf{r}') = (\hat{\mathbf{r}} - \hat{\mathbf{k}}^{inc}) \cdot \mathbf{r}' \tag{8}$$

3. THE GENERALIZED REFLECTION COEFFICIENTS

For the coated scatterers, the planar layered medium is depicted in Fig. 2. When the perpendicularly polarized wave is discussed here, the generalized reflection coefficients can be written as [1]:

$$\tilde{R}_{12} = R_{12} + \frac{T_{12}R_{23}T_{21}\,e^{2ik_{2z}(d_2-d_1)}}{1 - R_{21}R_{23}\,e^{2ik_{2z}(d_2-d_1)}} \tag{9}$$

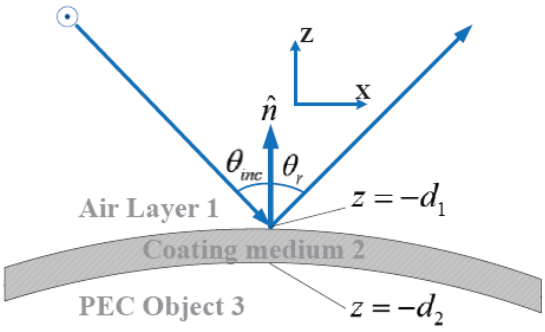

Figure 2. Reflection from a three-layer coated scatterers.

Note that

$$k_{iz}=\sqrt{k_i^2-k_x^2},\quad k_i^2=\omega^2\mu_i\varepsilon_i \tag{10}$$

$$R_{ij}=\frac{\mu_j k_{iz}-\mu_i k_{jz}}{\mu_j k_{iz}+\mu_i k_{jz}},\quad T_{ij}=\frac{2\mu_j k_{iz}}{\mu_j k_{iz}+\mu_i k_{jz}} \tag{11}$$

Here, $\tilde{R}_{12}$ is the generalized reflection coefficient for the one layer of coating between air half space and PEC scatterer that relates the amplitude of the upgoing wave to the amplitude of the downgoing wave in the air layer. It includes the effect of subsurface reflections as well as the reflections from the first interface. Also, ε_i and μ_i are the relative permittivity and permeability of the i-th medium, respectively. For the case of the parallel polarized wave incident on the medium, the generalized reflection coefficients can be written in a similar form.

4. THE QUADRATIC SURFACE SUBDIVISION TECHNOLOGY AND CLOSED-FORM FORMULATIONS FOR THE PO SCATTERED FIELDS

4.1. The Quadratic Surface Subdivision Technology

In contrast to the traditional planar surface meshing, the quadratic surface subdivision is adopted in this work. The effect of the surface subdivision proposed in this work is demonstrated in Fig. 3 [38, 39].

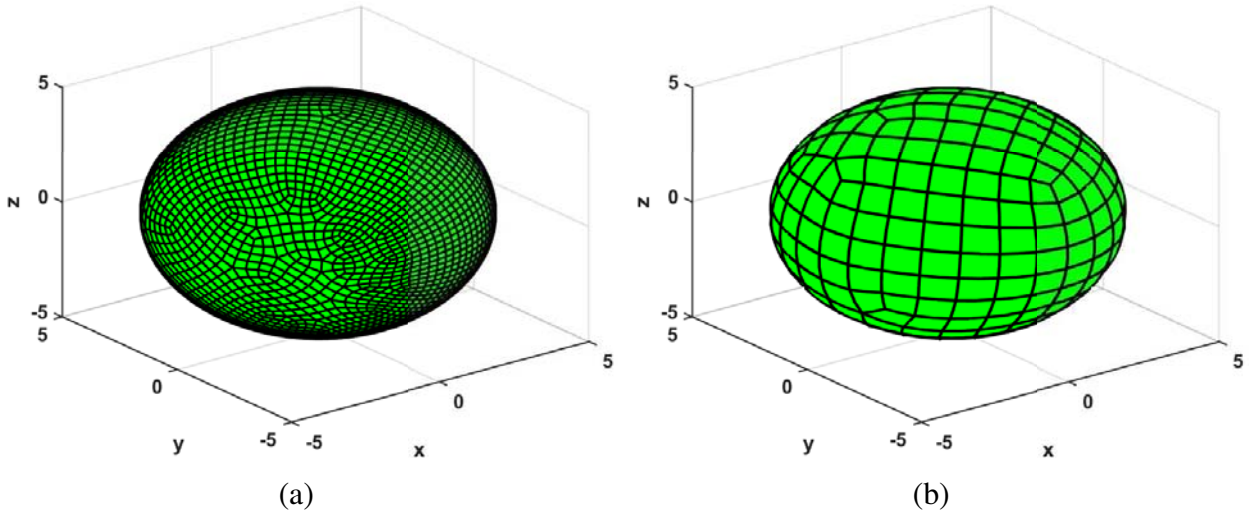

Figure 3. The discretization of the spherical scatterer. (a) With planar patches; (b) with quadratic patches.

We find that compared to planar patches, fewer quadratic patches can model the sphere with a high accuracy. Next, we can take advantage of the z-buffer technique to find the lit region of the considered scatterers. Hence, the PO scattered fields can be formulated as

$$\mathbf{E}^s(\mathbf{r}) \approx \sum_{n=1}^{N} \int_{\square_n} \mathbf{s}(\mathbf{r},\, \mathbf{r}') e^{-ikv(\mathbf{r},\mathbf{r}')} dS(\mathbf{r}') \tag{12}$$

where N is the number of the quadratic quadrilateral patches, and $\square_n$ is the n-th quadratic quadrilateral patch.

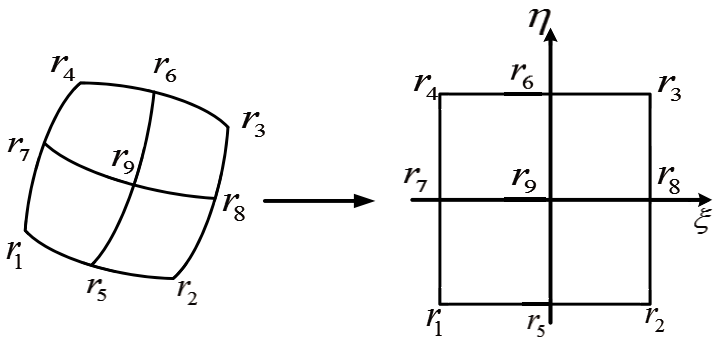

Figure 4. Transformation of the quadratic quadrilateral patch into a square patch in the parameter coordinate system.

In order to calculate the PO scattered fields accurately, the quadratic quadrilateral patches can be transformed into a square patch in the parametric coordinate system as shown in Fig. 4. The point on the surface can be represented by the polynomials with ξ and η as two parameters. The quadratic quadrilateral space $\mathbf{r}$ and the parameter coordinates (ξ, η) are related as

$$\mathbf{r}(\xi,\eta) = (x,y,z) = \sum_{i=1}^{8} N_i(\xi,\eta)\mathbf{r}_i' \tag{13}$$

where (ξ, η) and (x, y, z) are the parametric coordinates and spatial coordinates corresponding to any point on the quadratic quadrilateral patches, respectively. Also $\mathbf{r}_i'$ $(i = 1, \ldots, 8)$ represents the spatial location of the curved quadrilateral node. The shape function $N_i(\xi, \eta)$ can be expressed as

$$N_i(\xi,\eta) = \begin{cases} \dfrac{1}{4}(1+\xi_i\xi)(1+\eta_i\eta)(\xi_i\xi+\eta_i\eta-1), & i=1,2,3,4 \\ \dfrac{1}{2}(1-\xi^2)(1+\eta_i\eta), & i=5,6 \\ \dfrac{1}{2}(1-\eta^2)(1+\xi_i\xi), & i=7,8 \end{cases} \tag{14}$$

where (ξ_i, η_i) are the parametric coordinates of the i-th interpolation point in Fig. 4.

After the coordinate system transformation, the PO scattered field can be expressed as

$$\mathbf{E}^s(\mathbf{r}) \approx \sum_{n=1}^{N} \int_{-1}^{1}\int_{-1}^{1} \mathbf{s}(\xi,\eta) e^{-ikv(\xi,\eta)} d\xi d\eta \tag{15}$$

In order to calculate the PO surface integral over each quadratic quadrilateral patch efficiently, the Lagrange second order interpolation approximation polynomial was adopted. Since the governing equation of the quadratic quadrilateral patches is nonlinear, the second order vector polynomial amplitude function $\mathbf{P}_n(\xi, \eta)$ and the phase function $Q_n(\xi, \eta)$ can be chosen to approximate the original amplitude and phase functions, respectively. In each square patch, the five points r_1, r_5, r_2, r_8, r_3 are

chosen in the parametric coordinate system, so the closed-form formulas can be obtained by using the affine transformation. Then, the PO integral in the parameter domain can be written as

$$\mathbf{E}^s(\mathbf{r}) \approx \sum_{n=1}^{N} \int_{-1}^{1} \int_{-1}^{1} \mathbf{P}_n(\xi,\eta) e^{-ikQ_n(\xi,\eta)} d\xi d\eta \tag{16}$$

where

$$\begin{aligned} \mathbf{P}_n(\xi,\eta) &= \mathbf{\Gamma}_{n,1} + \mathbf{\Gamma}_{n,2}\xi + \mathbf{\Gamma}_{n,3}\eta + \mathbf{\Gamma}_{n,4}\xi^2 + \mathbf{\Gamma}_{n,5}\eta^2 \\ Q_n(\xi,\eta) &= \beta_{n,1} + \beta_{n,2}\xi + \beta_{n,3}\eta + \beta_{n,4}\xi^2 + \beta_{n,5}\eta^2 \end{aligned} \tag{17}$$

4.2. The Closed-Form Formulas for the PO Integral

In the parametric coordinate system, the PO integral can be written as

$$\mathbf{E}^s(\mathbf{r}) \approx \sum_{n=1}^{N} \int_{-1}^{1} \int_{-1}^{1} \mathbf{P}_n(\xi,\eta) e^{-ikQ_n(\xi,\eta)} d\xi d\eta \tag{18}$$

In order to calculate the PO surface integral, the phase function $\mathbf{Q}_n(\xi,\eta)$ can be transformed into the canonical form as $(\pm\xi^{'2} \pm \eta^{'2})$ after the affine transformation

$$Q_n(\xi,\eta) = \xi^{'2} + \eta^{'2} + \phi \tag{19}$$

The integration domain $d\xi d\eta$ in the parameter coordinate system can also be transformed as

$$d\xi' d\eta' = \psi d\xi d\eta$$

Since ϕ and ψ are constants, we can include them in an amplitude function $\mathbf{P}_n(\xi',\eta')$. In this way, the PO integral can be transformed as

$$\mathbf{E}^s(\mathbf{r}) \approx \sum_{n=1}^{N} \int_{L_{n,1}}^{L_{n,2}} \int_{L_{n,3}}^{L_{n,4}} \mathbf{P}'_n(\xi',\eta') e^{-ik(\pm\xi'^2 \pm \eta'^2)} d\xi' d\eta' = \sum_{n=1}^{N} \mathbf{I}_n \tag{20}$$

Here, the integration limit is changed to

$$\begin{aligned} L_{n,1} &= -\sqrt{|\beta_{n,4}|} + \frac{\beta_{n,3}}{2\sqrt{|\beta_{n,4}|}} \\ L_{n,2} &= \sqrt{|\beta_{n,4}|} + \frac{\beta_{n,2}}{2\sqrt{|\beta_{n,4}|}} \\ L_{n,3} &= -\sqrt{|\beta_{n,5}|} + \frac{\beta_{n,3}}{2\sqrt{|\beta_{n,5}|}} \\ L_{n,4} &= \sqrt{|\beta_{n,5}|} + \frac{\beta_{n,3}}{2\sqrt{|\beta_{n,5}|}} \end{aligned}$$

The integral $\mathbf{I}_n$ is calculated by means of the closed-form formulas. We deal with the general form PO integral as follows

$$I = \int_{L_1}^{L_2} \int_{L_3}^{L_4} P(\xi',\eta') e^{-ik(\pm\xi'^2 \pm \eta'^2)} d\xi' d\eta' \tag{21}$$

where

$$\mathbf{P}(\xi',\eta') = \boldsymbol{\alpha}_1 + \boldsymbol{\alpha}_2\xi' + \boldsymbol{\alpha}_3\eta' + \boldsymbol{\alpha}_4\xi^{'2} + \boldsymbol{\alpha}_5\eta^{'2} \tag{22}$$

With regard to this integral, we have

$$\begin{aligned} \int_a^b e^{-ikx^2} &= -\frac{1}{2}\sqrt{\frac{\pi}{ik}} \left(\mathrm{erfc}(\sqrt{ik}b) - \mathrm{erfc}(\sqrt{ik}a)\right) \\ \int_a^b e^{ikx^2} &= -\frac{1}{2}\sqrt{\frac{\pi}{-ik}} \left(\mathrm{erfc}(\sqrt{-ik}b) - \mathrm{erfc}(\sqrt{ik}a)\right) \end{aligned}$$

$$\begin{aligned}
\int_a^b xe^{-ikx^2} &= -\frac{1}{2ik}\left(e^{-ikb^2} - e^{-ika^2}\right) \\
\int_a^b xe^{ikx^2} &= \frac{1}{2ik}\left(e^{ikb^2} - e^{ika^2}\right) \\
\int_a^b x^2e^{-ikx^2} &= -\frac{1}{2ik}\left(be^{-ikb^2} - ae^{-ika^2} - \int_a^b e^{-ikx^2}dx\right) \\
\int_a^b x^2e^{ikx^2} &= \frac{1}{2ik}\left(be^{ikb^2} - ae^{ika^2} - \int_a^b e^{ikx^2}dx\right)
\end{aligned}$$

Supposing that the symbols of ξ' and η' are positive, the closed-form formula can be expressed as

$$\begin{aligned}
I &= (\alpha_1 I_1(L_1, L_2) + \alpha_2 I_3(L_1, L_2) + \alpha_4 I_2(L_1, L_2)) \cdot I_1(L_3, L_4) \\
&\quad + \alpha_3 I_1(L_1, L_2) I_3(L_3, L_4) + \alpha_5 I_1(L_1, L_2) I_2(L_3, L_4)
\end{aligned} \tag{23}$$

where

$$\begin{aligned}
I_1(a,b) &= -\frac{1}{2}\sqrt{\frac{\pi}{ik}}\left(\mathrm{erfc}(\sqrt{ik}b) - \mathrm{erfc}(\sqrt{ik}a)\right) \\
I_2(a,b) &= -\frac{1}{2ik}\left(be^{-ikb^2} - ae^{-ika^2} - I_1(a,b)\right) \\
I_3(a,b) &= -\frac{1}{2ik}\left(e^{-ikb^2} - e^{-ika^2}\right)
\end{aligned}$$

and

$$\mathrm{erfc}(z) = \frac{2}{\sqrt{\pi}}\int_z^\infty e^{-t^2}dt$$

Here, $\mathrm{erfc}(\cdot)$ is the complementary error function. Thus, the PO scattered fields in Eq. (21) can be calculated by using the closed-form formulas.

5. THE MULTILEVEL TECHNOLOGY

5.1. An Introduction to the Multilevel Approach

In this section, the multilevel technology is employed for the fast computation of the scattered electromagnetic (EM) field. The algorithm is based on the band limited nature of the contribution to the fields by subdomain $\overline{S}$. This means that the partial EM scattered field due to a subdomain $\overline{S}$, circumscribed by a smallest sphere with radius R, is a bandlimited function and can be sampled over a coarse grid with a sampling rate proportional to kR [34]. This property implies that the calculation aggregating the contributions by small subdomains requires fewer operations than the direct calculations of the EM scattered field of the total scatterer. The multilevel technology determines the number of scattered field samples to be calculated based on the electrical size of the scatterer [40]. The scattered field value at any point can be obtained by the sample interpolation. Hence, in order to reduce the electrical size of each target, a large-scale target structure is decomposed into a multilevel hierarchy of sub-regions that are closely connected with each other. In this manuscript, the octree decomposition of the entire scatterer is adopted. First, we use a cube to surround the scatterer. Then, the pre-set cubes are split into eight small ones through octree decomposition. In order to make full use of the multi-layer segmentation, we continue the above decomposition operation until the radius of the smallest sphere circumscribing the sub-domain is on the order of one wavelength. According to the domain decomposition in Fig. 5, the number of scattering patterns is decreased progressively from level 0 to level M. The size of the subdomain on the child level is about half of that on the parent's level. At the M-th level, the scatterer is decomposed into $O(N^2)$ sub-regions with an average size of 1λ at the highest frequency of interest. Next, we need to calculate the electromagnetic scattered field of each sub-domain separately. To obtain the total field from the partial contributions, the phase compensation, aggregation, and interpolation must be performed, from the coarse grids associated with the small subdomains to the

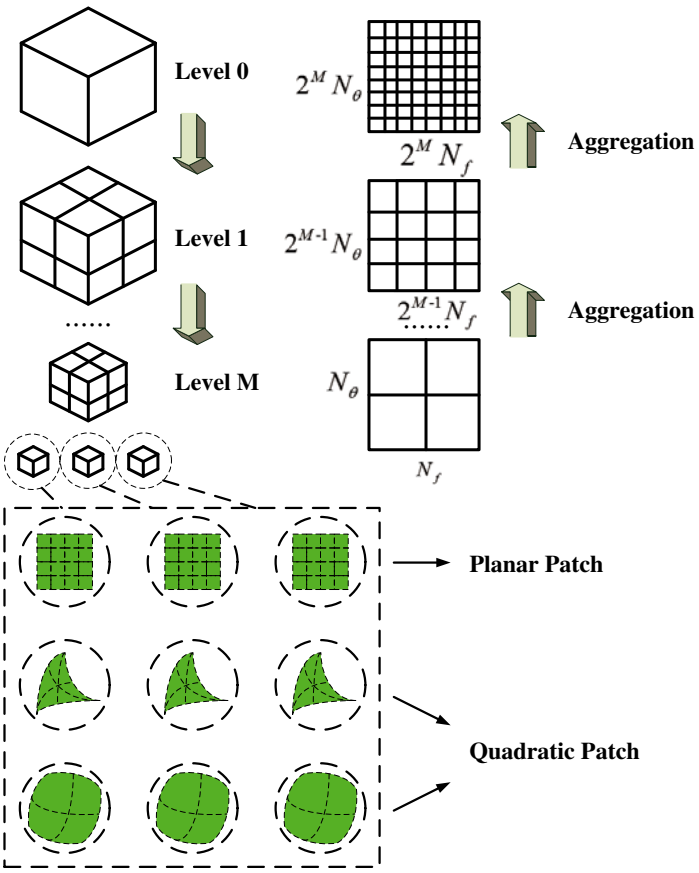

Figure 5. Schematic overview of the multilevel technology.

dense grid capturing the field of the entire scatterer gradually. The multilevel technology divides the target along $O(\log N)$ levels with $O(N^2)$ sub-regions at the last level. Apparently, the computational complexity can be effectively decreased to $O(N^2 \log N)$.

5.2. Domain Decomposition

As a preprocessing step of the multilevel computational sequence, we perform the domain decomposition process. Assuming that the surface of considered scatterer is S, let $\overline{S}_n^L$ denote the n-th ($n = 1, 2, \cdots, N^L$) subdomain of level L ($L = 0, 1, \cdots, M$), where $(M+1)$ is the total number of levels and N^L is the number of subdomains on level L. Obviously, $N^L = 8^L$ because the octree decomposition is adopted in this work. Only one subdomain is considered on the 0-th level, i.e., $\overline{S}_1^0 = S$, which represents the entire scatterer. Generally, a parent subdomain at each level can be decomposed into several children subdomains, i.e.,

$$\overline{S}_m^{L-1} = \bigcup_{n\,:\,P^L(n)=m} \overline{S}_n^L \tag{24}$$

where $P^L(n) = m$ means that the nth subdomain on level L is the sub-domain of the mth domain on the parent level $(L-1)$.

Let $\overline{R}_n^L$ and $\overline{\mathbf{r}}_n^L$ be the radius and the center of the smallest sphere circumscribing the subdomain $\overline{S}_n^L$, respectively. By adopting the octree subdivision, we expect that the diagonal length of the cube containing the child sundomain is half of that of the parent cube. Then, the radius of the domain on the parent level is twice as large as that on the child level, i.e.,

$$R_m^{L-1} = 2R_n^L, \quad P^L(n) = m \tag{25}$$

5.3. Phase Compensation and Interpolation

The PO integral can be expressed as follows

$$\mathbf{E}^s(\mathbf{r}) = \int_S \mathbf{A}(\theta, \varphi, \mathbf{r}') e^{-ik(\hat{\mathbf{k}}^s - \hat{\mathbf{k}}^i)\cdot \mathbf{r}'} dr' \tag{26}$$

When the high-frequency scattering characteristics are considered, that is, the wavenumber k is a large value, the amplitude term of the PO integral formula is a slowly varying function, while the phase term varies dramatically with the wavenumber k. The PO integrals from domain n on level M are highly oscillatory functions of frequency and aspect angles. If we consider the PO integration directly in the global coordinate system, it will introduce great difficulties to subsequent interpolation operation. In order to eliminate this difficulty, we can move from the global coordinate system to the local one which is centered on the subdomain as shown in Fig. 5. In the coordinate system centered at $\overline{\mathbf{r}}_n^M$, the PO radiation integral can be expressed as:

$$\mathbf{E}^s_{M,n}(\mathbf{r}) = \mathbf{e}^{-\mathbf{ik}(\hat{\mathbf{k}}^{\mathbf{s}} - \hat{\mathbf{k}}^{\mathbf{inc}})\cdot \overline{\mathbf{r}}^{\mathbf{M}}_{\mathbf{n}}} \int_{\overline{\mathbf{S}}^{\mathbf{M}}_{\mathbf{n}}} \mathbf{A}(\theta, \varphi, \mathbf{r}') \mathbf{e}^{-\mathbf{ik}(\hat{\mathbf{k}}^{\mathbf{s}} - \hat{\mathbf{k}}^{\mathbf{inc}})\cdot(\mathbf{r}' - \overline{\mathbf{r}}^{\mathbf{M}}_{\mathbf{n}})} \mathbf{dr}' \tag{27}$$

We assume that the size of the domain on the bottom level is about $\lambda = \frac{2\pi}{k_{\max}}$, then, the integral in Eq. (27) is slowly varying versus frequencies and aspect angles since $k_{\max}\|\mathbf{r}' - \overline{\mathbf{r}}_n^M\| \leq 2\pi$. The oscillatory factor is removed by multiplying $e^{ik(\hat{\mathbf{k}}^s - \hat{\mathbf{k}}^{inc})\cdot \overline{\mathbf{r}}_n^M}$, and the PO integral yields smooth results

$$\widetilde{\mathbf{E}}^s_{M,n} = \int_{\overline{S}_n^M} \mathbf{A}(\theta, \varphi, \mathbf{r}') e^{-ik\left(\hat{\mathbf{k}}^s - \hat{\mathbf{k}}^{inc}\right)\cdot\left(\mathbf{r}' - \overline{\mathbf{r}}_n^M\right)} d\mathbf{r}' \tag{28}$$

The phase factor $e^{-ik(\hat{\mathbf{k}}^s - \hat{\mathbf{k}}^{inc})\cdot \overline{\mathbf{r}}_n^M}$ in Eq. (27) can be interpreted as a shift of the origin of the coordinate system to the center of the sphere circumscribing the subdomain, $\overline{\mathbf{r}}_n^M$, this shift is important because it cancels the highly oscillationary phase variation as a function of frequency. Hence, the shift makes the radiation pattern amenable to the sampling and interpolation. Subsequently, we can compute the full radiation pattern by aggregating all the partial ones together.

Next, we need to consider the phase compensation and aggregation, the interpolation results for the dense grids should be multiplied by the factor of $e^{-ik(\hat{\mathbf{k}}^s - \hat{\mathbf{k}}^{inc})\cdot \overline{\mathbf{r}}_n^M}$. For the 0-th level, the scattering pattern can be obtained by aggregating the scattered fields of all the subdomains, i.e.,

$$\mathbf{E}(\theta, \varphi, \mathbf{r}') = \sum_{n=1}^{N^L} e^{-ik\left(\hat{\mathbf{k}}^s - \hat{\mathbf{k}}^i\right)\cdot \overline{\mathbf{r}}_n^M} \cdot \tilde{\mathbf{E}}^s_n(\theta, \varphi, \mathbf{r}') \tag{29}$$

The above equation includes the phase recovery term $e^{-ik(\hat{\mathbf{k}}^s - \hat{\mathbf{k}}^i)\cdot \overline{\mathbf{r}}_n^M}$ applied to the phase compensated field. The scattered field $\mathbf{E}^s_{M,n}(\theta, \varphi, \mathbf{r}')$ of each subdomain at the bottom $L = M$ level can be obtained through Eq. (27). Instead, based on the relationship between the parent level and the child level, the scattered fields for the dense grids from each domain on level L could be aggregated to obtain the results on level $(L-1)$, i.e.,

$$\tilde{\mathbf{E}}^s_{L-1,n}(\theta, \varphi, \mathbf{r}') = \sum_{n\,:\,P^L(n)=m} e^{ik(\hat{\mathbf{k}}^s - \hat{\mathbf{k}}^i)\cdot(\mathbf{r}_m^{L-1} - \mathbf{r}_n^L)} \tilde{\mathbf{E}}^s_{L,n}(\theta, \varphi, \mathbf{r}') \tag{30}$$

The scattering patterns on level 0 can be obtained by repeating the phase compensation and aggregation steps. The calculation of the unknown cannot be reduced if Eq. (30) is directly calculated by the Gaussian quadrature rule. Next, the interpolation operation is introduced.

Because of the slowly varying nature of the amplitude function of the PO scattered field, the PO integral can be considered as the aggregation of the exponential terms $e^{-ik(\hat{\mathbf{k}}^s - \hat{\mathbf{k}}^i)\cdot \mathbf{r}'}$. If we want to obtain the scattered fields at all frequencies using those at a small number of frequencies through the interpolation in the frequency domain, then according to the Nyquist sampling theorem, the frequency sampling interval Δf should satisfy the following condition

$$\Delta f \leq \frac{c}{4R}$$

where c is the speed of light in the free space. Therefore, the number of the frequency sampling points could be given by

$$N_f = \frac{\Omega_f 4R(f_{\max} - f_{\min})}{c} \tag{31}$$

where $\Omega_f > 1$ is the oversampling ratio. The PO integral is essentially a band-limited function with respect to angles θ and φ. Thus, in order to meet the preset accuracy and ensure that the scattered field under the fine grid $[\alpha_{\min}, \alpha_{\max}]$ ($\alpha = \theta$ or φ) obtained through sparse sampling interpolation, the number of angle samples could be calculated as follows

$$N_\alpha = \frac{\Omega_\alpha 4R(\alpha_{\max} - \alpha_{\min}) f_{\max}}{c}, \quad \alpha = \theta, \varphi \tag{32}$$

where Ω_α is the control parameter of sampling points on the angle domain and $\Omega_\alpha > 1$.

Following Eqs. (31) and (32), the frequency and angular samples are determined by the parameter R which is the radius of the sphere that circumscribe the scatterer. Based on the relationship between adjacent levels via Eq. (25), we double the grid density for frequencies and angles upon transition between the child level and the parent level respectively, i.e.,

$$N_\chi^{L-1} = 2N_\chi^L, \quad L \leq M, \quad \chi = f, \theta, \varphi \tag{33}$$

Once the sampling points are determined, the sparse coordinate system of each level can be expressed as $(f_m^L, \theta_i^L, \varphi_j^L)$, $m = 1, \ldots, N_f^L$, $i = 1, \ldots, N_i^L$, $j = 1, \ldots, N_j^L$. The scattered fields values at bottom level can be obtained on the coarsest grid coordinate system via (27), i.e.,

$$\mathbf{E}_{M,n}^s = \int_{\bar{S}_n^M} \mathbf{A}\left(\theta_i^M, \varphi_j^M, \mathbf{r}'\right) e^{-ik\left(\hat{\mathbf{k}}_{ij}^{s,M} - \hat{\mathbf{k}}^i\right)\cdot\left(\mathbf{r}' - \mathbf{r}_n^M\right)} dr' \tag{34}$$

for $n = 1, \ldots, N^M$, where $\hat{\mathbf{k}}_{ij}^{s,M} = \hat{\mathbf{k}}^s(\theta_i^M, \varphi_j^M)$. The radiation characteristic of subdomain m on level $(L-1)$ can be obtained by the interpolation process of its sub-levels through Eq. (30)

$$\mathbf{E}_{L-1,m}^s\left(\theta_i^{L-1}, \varphi_j^{L-1}, \mathbf{r}'\right) = \sum_{n:P^L(n)=m} e^{ik\left(\hat{\mathbf{k}}^s - \hat{\mathbf{k}}^i\right)\cdot\left(\mathbf{r}_m^{L-1} - \mathbf{r}_n^L\right)} \tilde{\mathbf{E}}_{L,n}^s\left(\theta_i^{L-1}, \varphi_j^{L-1}, \mathbf{r}'\right) \tag{35}$$

where

$$\tilde{\mathbf{E}}_{L,n}^s\left(\theta_i^{L-1}, \varphi_j^{L-1}, \mathbf{r}'\right) = \sum_{i':\theta_{i'}^L \in \psi_p^L(\theta_i^{L-1})} A_{ii'}^L \tilde{\mathbf{E}}_{L,n}^s\left(\theta_{i'}^L, \varphi_j^{L-1}, \mathbf{r}'\right) \tag{36}$$

and

$$\tilde{\mathbf{E}}_{L,n}^s\left(\theta_{i'}^L, \varphi_j^{L-1}, \mathbf{r}'\right) = \sum_{j':\varphi_{j'}^L \in \psi_p^L(\varphi_j^{L-1})} B_{jj'}^L \tilde{\mathbf{E}}_{L,n}^s\left(\theta_{i'}^L, \varphi_{j'}^L, \mathbf{r}'\right) \tag{37}$$

Here, Eqs. (36) and (37) represent the interpolation operation on the θ domain and φ domain, respectively. Also, $A_{ii'}^L$ and $B_{jj'}^L$ are their respective interpolation coefficients. $\psi_p^L(\cdot)$ represents the child level interpolation sampling points used in calculating the scattered electric field at a sampling point on the parent level. At the bottom level, for each sampling point, different from the planar subdivision technique in [35], the quadratic surface subdivision technology in Fig. 5 was taken to calculate the partial EM field contribution of the subdomains in the M-th level, as described in Section 4.

6. NUMERICAL EXPERIMENTS

The results of the experiments are briefly summarized to illustrate the accuracy and efficiency of the proposed algorithm. We compare the radar cross section (RCS) computed by using the multilevel fast PO algorithm (MLFPO) and the traditional Gordon's method. The processor of the HW platform we used in this work is Intel(R) Core(TM) $i7-4790$ CPU @3.60 GHz, and the memory is 8.00 GB.

6.1. Bistatic Case for the Coated Sphere Discretized by Using the Quadratic Quadrilateral Patches

First, to validate the accuracy of the MLFPO method, a PEC hemisphere shell with 0.05 m thick coating shown in Fig. 6 is considered. The radius of the hemisphere is 5 m, the relative permittivity of the coating material, ε, is 2.6, and the relative permeability, μ, is 1. The incident wave travels along the $-\hat{z}$ direction with the electric field $\hat{x}$ polarized. The operation frequency is 1 GHz. By using the Gordon's method [27, 28], 110,652 planar patches should be used to achieve high accuracy. However, only 2,131 quadratic patches are needed to achieve the same accuracy. Fig. 7 demonstrates the accuracy of the MLFPO algorithm showing the agreement of the results produced by the MLFPO, the Gordon's, the FPO, and the MLPO methods. The CPU time of the MLFPO method is 503.3 s, while the CPU time of the Gordon's method is about 14.2 h. One can see that the calculation time is greatly reduced, roughly 102 fold, by using the MLFPO method. Furthermore, the results are error-controllable. So, the MLFPO can be applied to RCS analysis.

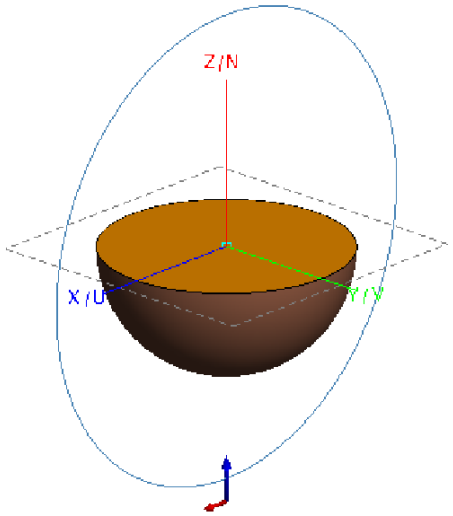

Figure 6. The coated hemispherical shell.

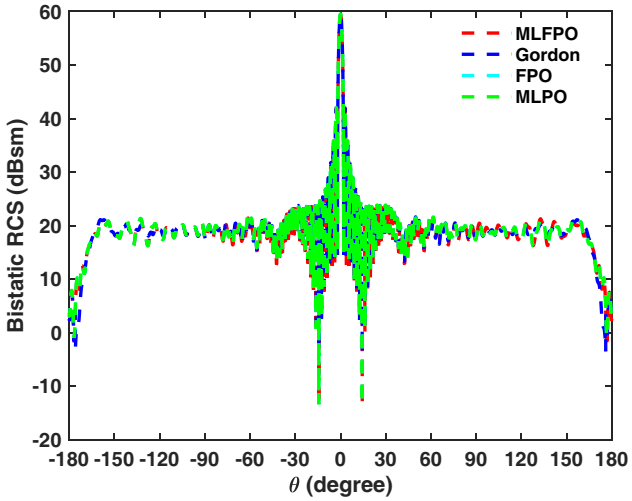

Figure 7. Compararison of the RCS of the coated hemispherical shell at $\phi = 0°$ computed by using the MLFPO, Gordon's, MLPO, and FPO method.

6.2. The Efficiency Comparison of the MLFPO and the Gordon's Methods

The accuracy of the MLFPO method has been proven in the above example. The RCS results of the MLFPO method agree well with those of the Gordon's method. Next, numerical experiments have been done to illustrate the computational efficiency of the MLFPO method. We consider the multi-frequencies cases for the coated sphere. Other information about the incident plane wave and the parameters of the coated sphere are the same as in the first example. The range of the frequencies is from 30 GHz to 90 GHz, for every single frequency, the range of the aspect angle θ is from 0 to π along the $\phi = 0$ cut. The number of the angular sampling points is 3601. The CPU time of every operating frequency is shown in Table 1. Fig. 8 shows the variation of the three algorithms' CPU time with the operating frequency. Apparently, the computation CPU time of the MLFPO method practically does not change with the increase of the operating frequency. On the other hand, the CPU time of the Gordon's method is dependent on the operating frequency heavily. When the high frequency is considered, the computational time of Gordon's method is much larger than that of the MLFPO proposed in this work. It is evident that the efficiency of the MLFPO proposed in this work is much better than that of the traditional Gordon's method.

Table 1. The CPU time for calculating the coated sphere by the MLFPO and the Gordon's methods for various frequencies.

Frequency (GHz)	MLFPO (min)	MLPO (min)	Gordon (min)
30	7.8	16.2	284.1
40	6.1	15.9	491.5
50	6.1	13.4	793.4
60	6.0	29.8	1149.1
70	6.0	63.5	1538.5
80	4.9	89.6	2050.1
90	4.8	47.5	2618.2

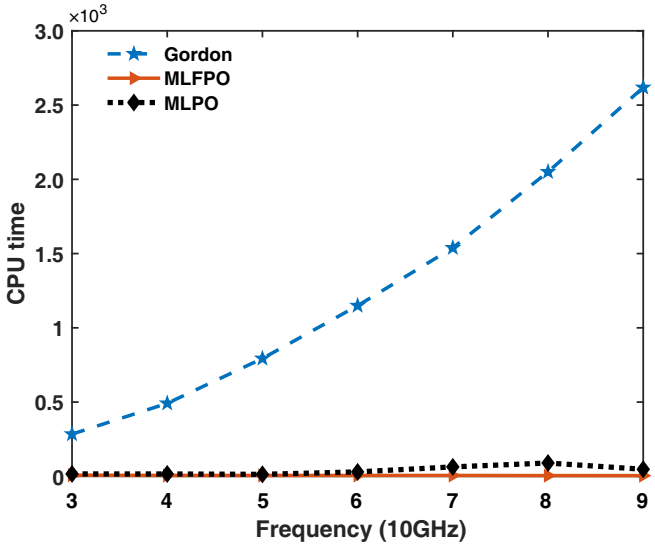

Figure 8. Comparison of the CPU time of the coated sphere by using the MLFPO algorithm, MLPO method and the Gordon's method.

6.3. Multi-Frequency and Multi-Angle Cases for the Coated Sphere

In order to demonstrate that the multilevel technology can reduce the complexity of calculating the scattered fields of multi-frequency and multi-angle cases effectively, we consider such computation scenarios for the coated sphere. The parameters of the coated sphere and the incident wave are the same as in the first example. The range of the frequencies is from 29 GHz to 30 GHz, and the range of the θ angles is from 170° to 190°. The number of the frequency sampling points is 48, and the number of aspect angle points is 1801. When the multilevel technology is used, the number of the frequency sampling and the aspect angle points are 28 and 144, respectively. The bistatic RCS results for the coated sphere are shown in Fig. 9. The results of the MLFPO method agree well with those from the Gordon's method. Hence, the accuracy of the MLFPO method proposed in this work can be guaranteed when the multi-frequency and multi-angle cases are considered. The CPU time of the MLFPO method is 808.6 s, but the CPU time of the Gordon's method is about 187.3 h, note that the CPU time of the MLFPO method is much smaller than that of the Gordon's method, which demonstrates that multilevel technology can reduce the computational complexity and improve the computational efficiency exceedingly well.

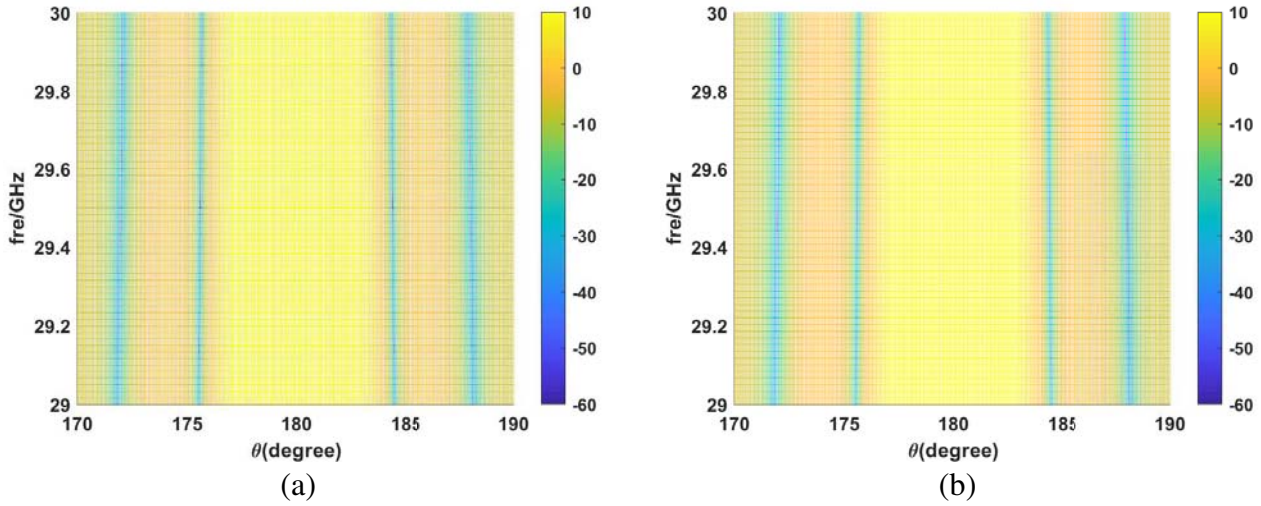

Figure 9. The multi-frequency and multi-angle bistatic RCS for coated sphere computed by using. (a) The MLFPO method, (b) the Gordon's method.

7. CONCLUSION

In this work, the MLFPO method is proposed for the simulation of multi-frequency and multi-angle electromagnetic scattering from electrically large coated scatterers. The quadratic discretization and the FPO method are adopted to decrease the computational complexity and, thus, speed up the computations. The multilevel technology is applied to reduce the computational complexity. The multilevel technology essentially reduces to the aggregation of the scattering patterns of increasingly larger subdomains, starting with the direct evaluation of the scattering characteristics of small surface subdomians and ending with the entire scatterer. Accurate and numerically efficient local interpolation schemes are the key to the efficient implementations of the multilevel domain decomposition approach. Numerical examples demonstrate that the proposed MLFPO method can reduce the computational workload significantly as compared to the traditional Gordon's method. Meanwhile, the accuracy can be gained. Hence, the method can be adopted to efficiently calculate the high frequency scattered fields of electrically large complex coated scatterers. Also, this algorithm can be applied in the RCS analysis.

REFERENCES

1. Chew, W. C., *Waves and Fields in Inhomogeneous Media*, IEEE Press, Piscataway, NJ, USA, 1995.
2. Kong, J. A., *Electromagnetic Wave Theory*, Wiley-Interscience, New York, NY, USA, 1990.
3. Balanis, C. A., *Advanced Engineering Electromagnetics*, Wiley, New York, 1989.
4. Jin, Y. Q., *Electromagnetic Scattering Modelling for Quantitative Remote Sensing*, World Science Press, Singapore, 2000.
5. Tang, L., J. A. Kong, and B. Shin, *Theory of Microwave Remote Sensing*, IEEE Press, New York, NJ, USA, 1995.
6. Harrington, R. F., *Field Computation by Moment Methods*, Wiley, Hoboken, NJ, USA, 2000.
7. Kulkarni, S., S. Uy, R. Lemdiasov, R. Ludwig, and S. Makarov, "MoM volume integral equation solution for an isolated metal-dielectric resonator with the edge-based basis functions," *IEEE Trans. Antennas Propag.*, Vol. 53, No. 4, 1566–1571, Apr. 2005.
8. Xiao, L., X. H. Huang, B. Z. Wang, G. Zheng, and P. Chen, "An efficient hybrid method of iterative MoM-PO and equivalent dipole-moment for scattering from electrically large objects," *IEEE Trans. Antennas Propag. Lett.*, Vol. 16, 1723–1726, 2017.

9. Jin, J. M., *The Finite Element Method in Electromagnetics*, 3rd edition, Wiley-IEEE Press, Hoboken, NJ, USA, 2014.
10. Taflove, A. and S. C. Hagness, *Computational Electrodynamics: The Finite-Difference Time-Domain Method*, 3rd edition, Artech House, Boston, NJ, USA, 2015.
11. Yao, J. J., S. Y. He, Y. H. Zhang, H. C. Yin, C. Wang, and G. Q. Zhu, "Evaluation of scattering from electrically large and complex PEC target coated with uniaxial electric anisotropic medium layer based on asymptotic solution in spectral domain," *IEEE Trans. Antennas Propag.*, Vol. 62, No. 4, 2175–2186, Apr. 2014.
12. Bhalla, R., H. Ling, J. Moore, D. J. Andersh, S. W. Lee, and J. Hughes, "3D scattering center representation of complex targets using the shooting and bouncing ray technique: A review," *IEEE Antennas Propag. Mag.*, Vol. 40, No. 5, 30–39, Oct. 1998.
13. Domingo, M., F. Rivas, J. Perez, R. P. Torres, and M. F. Catedra, "Computation of the RCS of complex bodies using NURBS surfaces," *IEEE Antennas Propag. Mag.*, Vol. 37, No. 6, 36–47, Dec. 1995.
14. Elking, D. M., J. M. Roedder, D. D. Car, and S. D. Alspach, "A review of high frequency radar cross section analysis capabilities at McDonnell Douglas Aerospace," *IEEE Antennas Propag. Mag.*, Vol. 37, No. 5, 33–43, Oct. 1995.
15. Wu, Y., L. J. Jiang, and W. C. Chew, "An efficient method for computing highly optics integral," *Progress In Electromagnetics Research*, Vol. 127, 211–257, 2012.
16. Wu, Y. M., L. J. Jiang, and W. C. Chew, "The numerical steepest descent path method for calculating physical optics integrals on smooth conducting quadratic surfaces," *IEEE Trans. Antennas Propag.*, Vol. 61, No. 8, 4183–4193, Aug. 2013.
17. Zhang, J., B. Xu, and T. J. Cui, "An alternative treatment of saddle stationary phase points in physical optics for smooth surfaces," *IEEE Trans. Antennas Propag.*, Vol. 62, No. 2, 986–991, Feb. 2014.
18. Fan, T. T., X. Zhou, and T. J. Cui, "Singularity-free contour-integral representations for physical-optics near-field backscattering problem," *IEEE Trans. Antennas Propag.*, Vol. 65, No. 2, 805–811, Feb. 2017.
19. Roudstein, M., Y. Brick, and A. Boag, "Multilevel physical optics algorithm for near-field double-bounce scattering," *IEEE Trans. Antennas Propag.*, Vol. 63, No. 11, 5015–5025, Nov. 2015.
20. Macdonald, H. M., "The effect produced by an obstacle on a train of electric waves," *Phil. Trans. Royal Soc. London, Series A, Math. Phys. Sci.*, Vol. 212, 299–337, 1913.
21. Hodges, R. E. and Y. Rahmat-Samii, "Evaluation of dielectric physical optics in electromagnetic scattering," *Symp. on Antennas and Propag. (IEEE APS1993)*, 1742–1745, 1993.
22. Li, N., W. C. Su, J. Yang, and L. J. Hu, "The bistatic formulae of dielectric objects in physical optics," *Symp. on Antennas and Propag. (IEEE APS1993)*, 1746–1749, 1993.
23. Cai, W. F., X. G. Liu, H. P. Guo, H. C. Yin, and P. K. Huang, "A concise expression for PO method on electromagnetic scattering by arbitrary shaped conducting targets with partially coating," *Environmental Electromagnetics (IEEE CEEM2003)*, 469–473, 2003.
24. Li, X., Y. Xie, and R. Yang, "High-frequency method for scattering from coated targets with electrically large size in half space," *IET Microw. Antennas Propag.*, Vol. 3, 181–186, Feb. 2009.
25. Liu, Z. L. and C. F. Wang, "Shooting and bouncing ray and physical optics for predicting the EM scattering of coated PEC objects," *Antennas and Propag. (IEEE APCAP12)*, 2012.
26. Mohammadzadeh, H., A. Z. Nezhad, Z. H. Firouzeh, and R. Safian, "Modified physical optics approximation and physical theory of diffraction for RCS calculation of dielectric coated PEC," *Symp. on Antennas and Propag. (IEEE APS2013)*, 1896–1897, 2013.
27. Gordon, W. B., "Far-field approximations to the Kirchoff-Helmholtz representations of scattered fields," *IEEE Trans. Antennas Propag.*, Vol. 23, No. 7, 590–592, Jul. 1975.
28. Gordon, W. B., "Near field calculations with far field formulas," *Proc. IEEE Trans. Antennas Propag. Soc.*, Vol. 2, No. 7, 950–953, Jul. 1996.

29. Ludwig, A. C., "Computation of radiation patterns involving numerical double integration," *IEEE Trans. Antennas Propag.*, Vol. 16, No. 6, 767–769, Nov. 1968.
30. Cátedra, M. F., C. Delgado, S. Luceri, and F. S. de Adana, "Efficient procedure for computing fields created by current modes," *Electron. Lett.*, Vol. 39, 763–764, May 2003.
31. Cátedra, M. F., C. Delgado, S. Luceri, O. G. Blanco, and F. S. de Adana, "Physical optics analysis of multiple interactions in large scatters using current modes," *IEEE Trans. Antennas Propag.*, Vol. 54, No. 3, 985–994, Mar. 2006.
32. Delgado, C., J. M. Gomez, and M. F. Cátedra, "Analytical field calculation involving current modes and quadratic phase expressions," *IEEE Trans. Antennas Propag.*, Vol. 55, No. 1, 233–240, Jan. 2007.
33. Boag, A., "A fast physical optics (FPO) algorithm for high frequency scattering," *IEEE Trans. Antennas Propag.*, Vol. 52, No. 1, 197–204, Jan. 2004.
34. Gendelman, A., Y. Brick, and A. Boag, "Multilevel physical optics algorithm for near field scattering," *IEEE Trans. Antennas Propag.*, Vol. 62, No. 8, 4325–4335, Aug. 2014.
35. Brick, Y. and A. Boag, "Multilevel nonuniform grid algorithm for acceleration of integral equation-based solvers for acoustic scattering," *IEEE Trans. Ultrason. Ferroelectr. Freq. Control*, Vol. 57, No. 1, 262–273, Jan. 2010.
36. Boag, A., "A fast iterative physical optics (FIPO) algorithm based on nonuniform polar grid interpolation," *Microw. Opt. Technol. Lett.*, Vol. 35, No. 3, 240–244, Nov. 2002.
37. Boag, A. and E. Michielssen, "A fast physical optics (FPO) algorithm for double-bounce scattering," *IEEE Trans. Antennas Propag.*, Vol. 52, No. 1, 205–212, Jan. 2004.
38. Song, J. M. and W. C. Chew, "Moment method solution using parameter geometry," *IEEE Trans. Antennas Propag.*, Vol. 3, 2242–2245, Jun. 1994.
39. Li, J., L. J. Jiang, and B. Shanker, "Generalized Debye sources-based EFIE solver on subdivision surfaces," *IEEE Trans. Antennas Propag.*, Vol. 65, No. 10, 5376–5386, Oct. 2017.
40. Bucci, O. M. and G. Franceschetti, "On the spatial bandwidth of scattered fields," *IEEE Trans. Antennas Propag.*, Vol. 35, No. 12, 1445–1455, Dec. 1987.